



pubs.acs.org/acsaom Forum Article

# Nonthermal Plasma Synthesis of Composition-Tunable Silicon Nitride Nanoparticle Films for Passive Radiative Cooling

Gunnar Nelson, Himashi P. Andaraarachchi, Julian Held, Mohammad Ali Eslamisaray, Ognjen Ilic, and Uwe Kortshagen\*



Cite This: ACS Appl. Opt. Mater. 2024, 2, 935-944



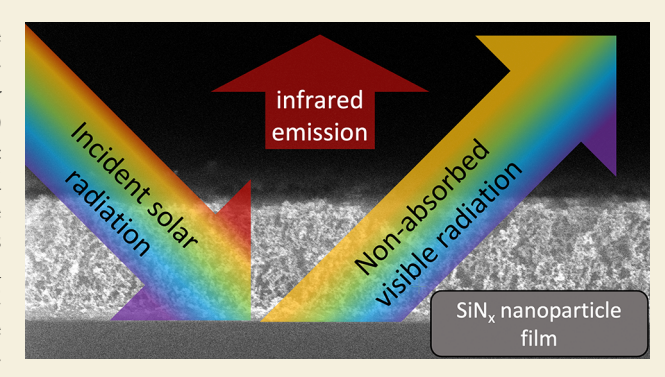
**ACCESS** I

III Metrics & More

Article Recommendations

s) Supporting Information

**ABSTRACT:** Passive radiative cooling (PRC) technologies have seen growing attention due to the increasing need for scalable, low-cost, and low-maintenance cooling devices. PRC devices work by minimizing the absorption of light in the visible spectrum (300–700 nm) while optimizing for high emissivity in the infrared atmospheric transmission window (8–14  $\mu$ m). However, identifying and synthesizing a material or material structure with these precise properties have been found to be challenging. Recently, simulations of silicon nitride (SiN<sub>x</sub>) nanoparticle films showed potential significant cooling power improvements over current PRC structures. In this work, we show a scalable, single step, and tunable synthesis technique to produce such homogeneous SiN<sub>x</sub> nanoparticle films. By using SiH<sub>4</sub>, Ar, and N<sub>2</sub> injected into nonthermal



plasma, the nanoparticle composition can be tuned with plasma power. Characterizing the optical properties of the films, we observe high infrared absorption and visible transparency, as required for PRC. The film composition was found to be tunable between stoichiometric Si<sub>3</sub>N<sub>4</sub> and nitrogen-poor SiN<sub>x</sub>, depending only on the plasma power. Finally, high plasma powers lead to silicon nanocrystal precipitation, suggesting an optimal plasma power for PRC film formation.

KEYWORDS: Silicon-Nitride, Nanoparticles, Nonthermal Plasma, Radiative Cooling, Thin Film Deposition, Plasma Chemistry

## 1. INTRODUCTION

Air cooling is the fastest growing use of energy in buildings, and demand is expected to triple by 2050. Passive radiative cooling (PRC) devices are a promising method to lower this energy cost without concern about additional energy input or intensive maintenance.<sup>2–8</sup> Optical PRC technologies generally consist of thin-film stacks or photonic structures upon a reflective substrate which minimizes solar absorption while maintaining high absorption/emissivity in the infrared (IR) atmospheric transmission window  $(8-14 \mu m)^9$ . In this spectral region, atmospheric gases absorb very little terrestrial emission, allowing for energy to pass through the atmosphere into space. If the radiation from the IR emitter (within 8–14  $\mu$ m) is greater than radiative and nonradiative heating sources, e.g., solar absorption, convection, etc., the device will cool below ambient temperature. Thus, a PRC device needs to achieve high IR emission, as well as minimized absorption in the visible spectrum. Furthermore, a proposed PRC device should aim to minimize impedance mismatch with free space as an abrupt optical medium change will induce Fresnel reflections, thus lowering potential cooling power. Thin-film based PRC devices have a narrow array of usable materials for reducing this impedance mismatch and photonic structures require time and energy intensive patterning techniques. 6,10,11 Recently,

Wray et al. simulated nanoparticle (NP) layers of stoichiometric silicon nitride ( $\mathrm{Si}_3\mathrm{N}_4$ ) and silicon dioxide ( $\mathrm{SiO}_2$ ) upon a silver back reflector and demonstrated an up to 50% increase in cooling power compared to other current PRC technologies. <sup>12</sup> This improvement originates from the NP films' unique advantages of optical tunability and improved optical coupling to free space.

Since NP films can be treated as an effective medium with a complex refractive index bounded by air and the NP material optical properties, tuning the porosity of the film allows for direct tuning of the films' optical properties. Furthermore, the random nature of NP deposition generally prevents phase preservation within the film therefore reducing Fresnel reflections from the air—NP film interface. As a result, NP films have improved optical coupling to free space, as well as increased polarization, angle, and wavelength independence compared to conventional thin films.

Special Issue: Optical Materials for Radiative Cooling

Received: July 28, 2023
Revised: November 4, 2023
Accepted: November 6, 2023
Published: November 30, 2023





Thus, following the theoretical work by Wray et al., we aimed to fabricate these optical NP films. Synthesizing high purity  $\mathrm{SiO}_2$  NPs at scale is possible through a variety of well-established techniques. Stoichiometric  $\mathrm{Si}_3\mathrm{N}_4$  is a well-known PRC film candidate with high emission in the atmospheric transmission window, no absorption in the visible spectrum, and high thermal and mechanical stability. However, silicon-nitride is inherently a nonmonolithic material as its stoichiometry varies significantly with the synthesis method and therefore the material is generally denotated as  $\mathrm{SiN}_x$  indicating a variable nitrogen content.  $\mathrm{SiN}_x$  thin film deposition has been extensively studied as these films have myriad applications ranging from passivation layers for solar cells to high-temperature structural coatings. However, bottom-up  $\mathrm{SiN}_x$  NP synthesis has not yet been thoroughly examined.

Recent work by Chae et al.  $^{24}$  and Kilian and Wiggers  $^{25}$  on silicon NP-based battery anodes have demonstrated a high-throughput  $\mathrm{SiN}_x$  NP production method via high-temperature, gas-phase techniques. These NPs were  $\sim 50-100$  nm in diameter with a wide range of chemical compositions. This synthesis technique was successfully employed to improve the stability of a silicon battery anode from nitrogen inclusion within the NPs. However, for optical applications, a more precise and controllable synthesis method is necessary for particles to have uniform optical properties, so the film itself can be entirely transparent.

Nonthermal plasma synthesis is a promising fabrication technique for a vast array of nanomaterials. Nonthermal plasmas provide a strong nonequilibrium environment, with mean electron temperatures of a few 10,000 K while the gas molecules and ions remain close to room temperature. This nonequilibrium characteristic allows for new synthesis pathways far from chemical equilibrium. High-energy electrons can easily dissociate injected gas-phase precursors, and the resulting free radicals can recombine to form solid NPs. Furthermore, NPs within the plasma are usually negatively charged, which means that particle agglomeration is strongly suppressed by Coulomb forces between particles. As such, nonthermal plasma synthesis has been found to be able to produce highly monodisperse NPs. 26-28 Additionally, NP films can be directly deposited from the reactor without needing solvents or adhesives. To this end, particles are extracted from the reactor through a nozzle and captured on a substrate by impact deposition, enabled by the pressure differential between the plasma (upstream) and beneath the nozzle in a deposition chamber (downstream). Hunter et al.<sup>29</sup> and Mandal et al.<sup>31</sup> have shown promising results using this method for synthesis of Si/SiN<sub>x</sub> core/shell NPs to prevent surface oxidation for optoelectronic applications. This work aims to build on the previous studies to produce composition-tunable, homogeneous SiN, NPs in this single-step, all gas-phase approach.

Typical gas-phase synthesis approaches for  $SiN_{xy}$  such as plasma enhanced chemical vapor deposition (PECVD) or pyrolysis, use ammonia (NH<sub>3</sub>) as the nitrogen precursor, since NH<sub>3</sub> has a low N–H bond energy (338 kJ/mol, 3.5 eV/atom). Thus, control of the nitrogen content of NPs can be achieved by varying the ratio between the silicon precursor and NH<sub>3</sub> flow rates. However, hydrogen will then be incorporated into the synthesized  $SiN_x$  NPs at a rate proportional to the NH<sub>3</sub> flow rate. N–H bonds within the material can have significant IR absorption outside of the desired atmospheric transmission window of 8–14  $\mu$ m.  $^{31,32}$ 

In this study, we instead use diatomic nitrogen  $(N_2)$  as the nitrogen precursor to reduce the film's hydrogen content. In this case, the formation of stoichiometric  $Si_3N_4$  can occur either directly due to  $N_2$  molecules or from atomic nitrogen formed by dissociation. The reaction with molecular nitrogen usually requires temperatures of around 1600 K, which are much larger than the typical gas temperatures of 300 to 400 K expected under our conditions. However, the reaction might still occur due to the high vibrational temperatures of molecules in plasmas or on the hot surface of already formed NPs. The reaction with atomic nitrogen first requires the dissociation of the diatomic nitrogen precursor (956 kJ/mol,  $10 \, \text{eV/atom}$ ), due to either impact of highly energetic electrons or vibrational ladder climbing.

However, for both reaction pathways, varying the N<sub>2</sub> concentration during the synthesis is unlikely to allow for a predictable control of the nitrogen content in the SiN<sub>x</sub> films. This is because any increase in molecular nitrogen concentration inside the plasma causes increased electron energy losses due to excitation of vibrational and rotational energy states of the molecules. Thus, increasing the molecular nitrogen content will usually lower the mean electron energy and, therefore, both the rate of molecule dissociation as well as the vibrational temperature of molecules. Therefore, increasing the molecular nitrogen concentration could potentially lower the nitrogen content of the particles instead of increasing it. Thus, we will instead work with a constant gas composition while varying the plasma power and thus the mean electron energy and electron density. This allows us to control the rate of nitrogen reactivity, thus allowing us to vary the nitrogen concentration of the SiN<sub>x</sub> films.

Using plasma power as a tuning parameter, in this work we will demonstrate the synthesis of fully transparent films of stoichiometric  $\mathrm{Si_3N_4}$  NPs with precisely tunable chemical and optical properties and high emissivity in the infrared atmospheric transmission window between 8 and 14  $\mu \mathrm{m}$  for PRC applications.

## 2. METHODOLOGY

Amorphous  $SiN_x$  NPs were produced in a single-step process, using a flow-through nonthermal plasma reactor developed in our lab. <sup>26,33</sup> A diagram of the reactor can be seen in Figure 1.

Silane (SiH<sub>4</sub>), argon (Ar), and nitrogen (N<sub>2</sub>) enter the reactor at the top ①, flowing into a 7/8 in. inner-diameter quartz tube at flow rates of 0.24, 38, and 1 sccm, respectively. Reactor pressure was maintained at 1.3 Torr (173 Pa). The 13.56 MHz radiofrequency (RF) signal was applied to a 10 mm wide copper ring on the outside of the quartz tube over a self-built impedance matching network. The plasma was operated at powers ranging from 10 to 90 W, as reported by the power supply (AG 0113 T&C Power Conversion). As Figure 1 shows, the powered electrode was located about 10 mm above the lower vacuum fitting on the quartz tube, which acts as the ground. A secondary gas flow of 5 sccm of N2 enters the reactor from the bottom in the plasma afterglow region 2. The flow is inserted concentrically using a gas shower constructed from a stainless-steel fitting with 16 1 mm holes spaced evenly within the circumference of the reactor. This secondary N2 flow ensures that the only limiting factor in terms of overall nitrogen content in the SiN<sub>x</sub> NPs is plasma power and not available diatomic nitrogen molecules. The overall constant N2 flow rate was split into flow from the top and the bottom, as increased N<sub>2</sub> flows from the top were found

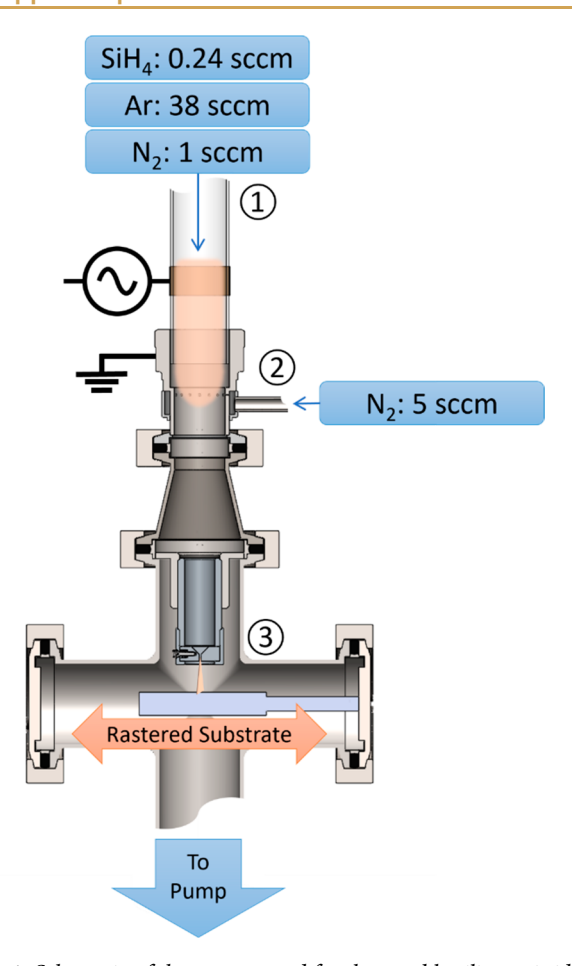


Figure 1. Schematic of the reactor used for the tunable silicon nitride nanoparticle synthesis. Primary gas mixture enters the reactor through the top  $\odot$ . Particles begin nucleation around the powered electrode placed  $\sim 1$  cm from the lower vacuum fitting. Secondary nitrogen enters through a side arm fitting toroidally into the chamber  $\odot$ . Particles accelerate through a nozzle to be ballistically impacted onto a rastered substrate  $\odot$ . Optical emission spectroscopy data was sampled from the plasma region between the powered electrode and the lower vacuum fitting.

to quench the plasma and narrow the compositional tuning range of the synthesized particles. In this way, we aim to keep the molecular nitrogen concentration lower at the top of the reactor to allow for efficient dissociation of the silicon precursor and the onset of particle nucleation, whereas a higher nitrogen content at the bottom will lead to increased nitrogen incorporation into the NPs as they move through the reactor.

Nanoparticles begin to nucleate at the beginning of the plasma region and continue growing as the gas drag force pushes the particles downward. The physical mechanisms behind particle growth and nucleation have been described elsewhere. The particles then accelerate through a slit nozzle of dimensions 0.5 mm  $\times$  12 mm. The distance from the nozzle to the substrate was 2 mm. Particles were deposited on a continuously rastered substrate, thus creating a film of homogeneous thickness. The substrate was moved at a rate of  $\sim$ 20 mm/s, and sample area was chosen between 0.5 to 3 cm in length depending on what was required for characterization.

## 2.1. Characterization Techniques

To measure the absorbance of the deposited NP films, ultraviolet—visible (UV—vis) absorption spectroscopy was performed with a Cary 7000 in the range from 350 to 800 nm. Samples were deposited on 25 mm  $\times$  75 mm BK7 glass slides for 30 raster passes. The Diffuse Reflectance Attachment (DRA) was used to measure total reflection and total transmission of the sample using an integrating sphere. Total reflection was measured by angling the sample  $<5^{\circ}$  at the back aperture of the integrating sphere. Total transmission was measured by mounting the sample in front of the entrance to the integrating sphere while plugging the back aperture with a Teflon puck.

Fourier transform infrared spectroscopy (FTIR) was performed with a Bruker ALPHA FTIR in diffuse reflectance mode in a nitrogen-filled glovebox. Samples were deposited for 30 raster passes on gold-plated silicon wafers. Samples were transferred air-free into a glovebox containing the FTIR spectrometer to capture as-deposited IR properties.

From the relative absorption A, measured by FTIR, the absorbance of the samples normalized to film thickness was calculated as  $\mu = -\ln(1-A)/d$ , where d is the thickness of the samples.

Sample thickness was measured via cross sectional scanning electron microscopy (SEM) using an FEI Helios NanoLab G4 instrument with an accelerating voltage of 2 kV (Figure S1). Samples were deposited on silicon wafers and then cleaved in half to be mounted vertically in the SEM. Before imaging, 5 nm of Pt was deposited upon the samples to improve contrast.

X-ray photoelectron spectroscopy (XPS) was performed using a PHI Versaprobe III instrument with a monochromatic Al K $\alpha$  anode X-ray source (photon energy = 1486.6 eV) and a hemispherical analyzer. Carbon 1s peak at 284.6 eV was used as a reference. Survey and high-resolution scans were acquired with 280 and 55 eV per pass, respectively. Data were acquired with the PHI Smartsoft XPS package and analyzed with PHI Multipack v9.0. Samples were transferred air-free from a nitrogen-filled glovebox to the XPS instrument to minimize the oxygen signal in the resulting XPS spectra.

Transmission electron microscopy (TEM) was performed using a Thermo Scientific FEI Talos F200x transmission electroscope operating at an accelerating voltage of 200 kV. TEM samples were collected directly on thin C coated Cu grids directly. Selective area diffraction pattern (SAED) and lattice parameters were analyzed using ImageJ.<sup>35</sup>

The particle growth process was characterized by using optical emission spectroscopy (OES). The plasma emission was observed at just below the powered electrode. The light was coupled into an optical fiber (Avantes FC-UVIR600-2) and guided to the entrance slit (25  $\mu$ m) of a plane grating spectrograph (Newport Oriel M260i) with a focal length of 260 mm and a grating with 1800 lines/mm. In this configuration, the CCD camera (Newport Oriel InstaSpec X 78234) can record about an 80 nm wide part of the emission spectrum. Thus, multiple measurements at different wavelength positions were needed for each plasma setting. To ensure the plasma conditions were constant for each of these measurements, the data were acquired as fast as possible by programmatically controlling the spectrometer and camera. Afterward, optical emission lines were fitted with a pseudo-Voigt profile to obtain the line intensity. For molecular species (N2 and NH), fitting was performed using Massive OES yielding rotational and vibrational temperatures as well as

intensities.<sup>36–38</sup> Since both band structures overlapped, the sum of both molecular bands was calculated and fitted to the measurement. For the argon neutral intensity, two emission lines were fitted at the same time, and the sum of the obtained intensities was used. The evaluated emission lines and bands are listed in Table 1.

Table 1. Optical Emission Lines or Bands That Were Investigated in This  $Study^a$ 

Species	Transition	Wavelength [nm]
Ar	$^{2}[1/2] \rightarrow ^{2}[1/2]^{\circ}$	750.387
Ar	$^{2}[1/2] \rightarrow ^{2}[3/2]^{\circ}$	751.465
Ar+	$^{2}\mathrm{P}^{\circ}\rightarrow^{2}\mathrm{P}$	476.486
Н	$4 \rightarrow 2$	486.135
Si	$^{1}P^{\circ} \rightarrow {^{1}D}$	288.158
N	${}^{4}P^{\circ}J = 5/2 \rightarrow {}^{4}PJ = 5/2$	821.634
$N_2$	$C^3\Pi \rightarrow B^3\Pi$ , $\Delta \nu = 0$	337
NH	$A^3\Pi \to X^3\Sigma$	336

<sup>a</sup>For the argon neutral intensity, two emission lines were fitted at the same time, and the sum of the obtained intensities was used. The molecular bands of  $N_2$  and NH were found to overlap, so the sum of both calculated band structures was fitted to the measurements.

## 3. RESULTS

## 3.1. Optical Properties

The nanoparticle (NP) films were first investigated for their transparency for light in the visible wavelength range, which is an important requirement for the application for passive radiative cooling (PRC), since minimized absorption within the visible spectrum prevents parasitic heating from overtaking the cooling power at a specific temperature. Stoichiometric or near-stoichiometric  $\mathrm{SiN}_x$  is transparent in nature, so that we expect the transparency of the films to vary with the nitrogen content of the synthesized NPs.

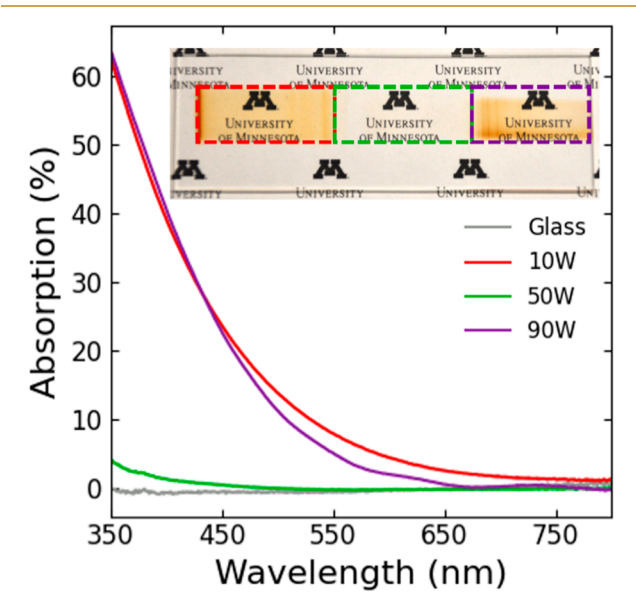
The NP films were deposited at different plasma powers but with constant flow rates and gas composition. The films were deposited for 60 s onto a glass slide and then positioned above a patterned surface, as is shown in Figure 2. The deposited films will slightly overlap on the edge of each sample deposition, leading to a thicker layer and less transparency. Thus, we will only regard the regions marked by the gray dotted outlines, where the films do not overlap.

Figure 2 shows that films deposited at 10 and 20 W are brown and not transparent. The 30 W film is transparent, but

some tint remains. In contrast, the films deposited with plasma powers between 40 and 70 W appear completely transparent. For higher powers, the brown color returns, making the samples less transparent. The brown color in the films is typically indicative of a higher silicon content. (Logo reproduced with permission of the University of Minnesota).

In order to confirm the suspected SiNx composition, UV—vis absorption spectroscopy was performed to measure the absorption of visible light from the deposited films.

Figure 3 shows the absorption in the wavelength range of 350-800 nm for  $SiN_x$  nanoparticle films deposited at low,



**Figure 3.** Absorption from 350 to 800 nm of samples deposited for 30 passes each at 10, 50, and 90 W of plasma power. A top-down photograph is shown to qualitatively highlight the absorption differences.

medium, and high powers (10, 50, and 90 W) on a 1.2 mm thick BK7 glass microscope slide measuring  $1 \times 2$  in. Both the 10 and 90 W samples exhibit absorption at lower wavelengths but are mostly transparent above 650 nm. This explains the red-brown appearance of the films at these powers, as seen in the photo at the top of the figure. (Logo reproduced with permission of the University of Minnesota).

The 50 W sample shows high transparency, with a minor absorption only below 475 nm. These dramatically different absorption profiles can be clearly seen in the top-down

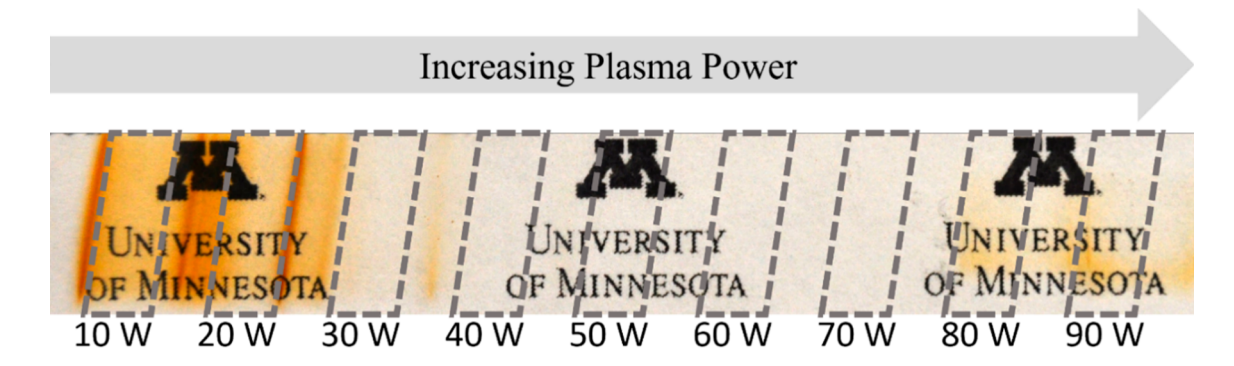


Figure 2. Top-down photo of sample set showing the transition between absorbing-transparent-absorbing SiNx nanoparticles with an increase in plasma power. The dotted gray boxes indicate sample area as labeled below.

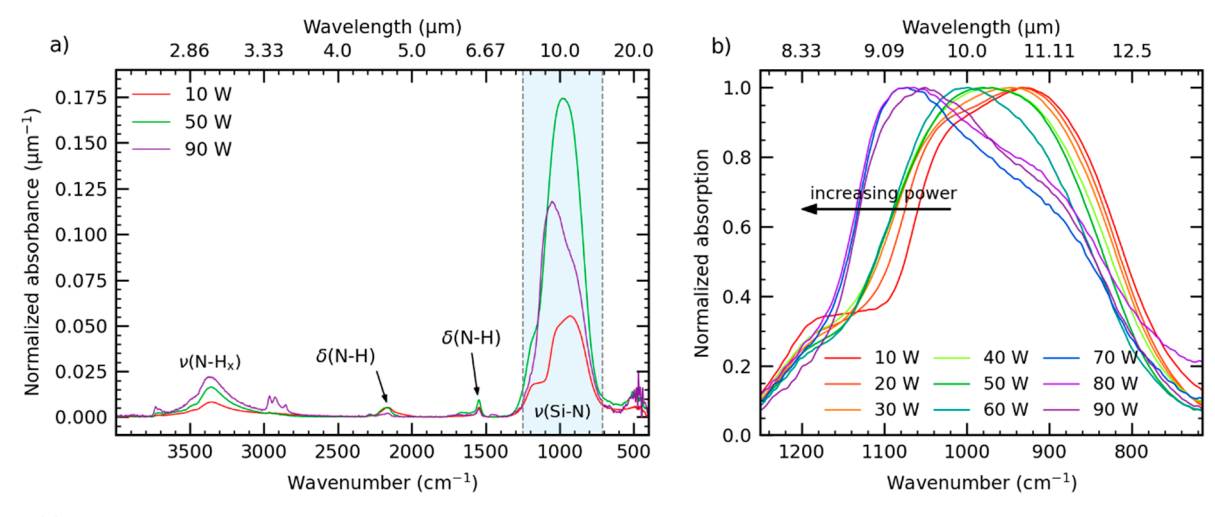


Figure 4. (a) Absorbance normalized to the film thickness of samples deposited at 10 W, 50 and 90 W of plasma power from 4000 to 400 cm<sup>-1</sup>. The highlighted area corresponds to the atmospheric transmission window (8–14  $\mu$ m). (b) Absorption of the full sample set from 10 to 90 W within the atmospheric transmission window, individually normalized to the maximum value.

photograph inset in Figure 3. As is evident from the photograph and absorption spectra, the sample deposited at 50 W shows the lowest absorption in the visible spectrum.

From Figures 2 and 3, it becomes clear that the NP films deposited at plasma powers of around 50 W are transparent for visible light, while lower and higher plasma powers yield films that absorb light of wavelengths below 650 nm. This trend can be explained by the nitrogen concentration inside the NP films, with the sample deposited at 50 W containing close to stoichiometric Si<sub>3</sub>N<sub>4</sub> NPs. Since the nitrogen concentration in the films is expected to increase with plasma power, the high absorption of the 10 W sample is likely due to the film being composed of silicon rich SiN<sub>x</sub> NPs. High absorption reemerges at high powers (90 W sample) due to silicon nanocrystal precipitation, as we discuss below. Our results indicate that high absorption is attributed to changes in composition and not film thickness: e.g., the high-power 90W sample is the thinnest of the three samples for the same deposition time (Figure S1).

Another important requirement for PRC applications is a high emissivity in the atmospheric transmission window of 8 to 14  $\mu$ m. Thus, we performed FTIR to measure absorption in the infrared region, which is equal to the emissivity, as well as reveal information about the surface composition of the NPs.

Figure 4a shows the film thickness-normalized absorbance of  $SiN_x$  NP samples produced at plasma powers of 10, 50, and 90 W, as measured using FTIR. The strongest absorption feature are observed around 800-1150 cm<sup>-1</sup> corresponds to the Si-N asymmetric stretching vibrations ( $\nu(Si-N)$ ) confirming the formation of SiN<sub>x</sub> at all powers. The shoulder observed at 1200 cm<sup>-1</sup> and the peak at 1550 cm<sup>-1</sup> are both caused by N-H vibrational modes ( $\delta(N-H)$ ). The peak at 2150 cm<sup>-1</sup> corresponds to the Si-H<sub>x</sub> stretching vibrations ( $\nu$ (Si-H<sub>x</sub>)). The main absorption feature located between 1250 cm<sup>-1</sup> and 700 cm<sup>-1</sup>, indicated by the blue shaded region in Figure 4a, correlates to the atmospheric transmission window of 8 to 14  $\mu$ m. In comparison, the other absorbance peaks detected by FTIR have heights of only between 10% and 20% of the absorption inside the atmospheric transmission window, depending on plasma power. That all of these peaks originate from hydrogen incorporated into the NPs highlights the importance of a low hydrogen concentration during the

synthesis, achieved here using molecular nitrogen as the nitrogen source instead of the more commonly used ammonia. The remaining hydrogen incorporated into the NPs likely originates from silane ( $SiH_4$ ) used as the silicon precursor.

Within the atmospheric transmission window, the absorbance reaches values of 0.175  $\mu m^{-1}$  in the case of the sample deposited at 50 W, compared to only 0.055  $\mu m^{-1}$  and 0.120  $\mu m^{-1}$ , for the 10 and 90 W samples, respectively. In contrast, the peak normalized absorbance values for conventional bulk SiN films typically fall within the range of 1–1.4  $\mu m^{-1.39-41}$  However, it should be noted that the fill factor of our NP films are estimated to be around 25%, 42 which explains part of this difference.

The shift in the Si-N stretching vibrations peak shown in Figure 4b indicates that the composition of SiN, can be tuned with plasma power. The figure shows an enlarged view of the absorption inside the atmospheric transmission window. Clearly, the absorption peak of Si-N shifts toward higher wavenumbers with increasing plasma power. For low plasma powers from 10 to 30 W, the absorption feature peaks around 915-920 cm<sup>-1</sup>, which is consistent with Si-rich SiN<sub>r</sub> as reported in the literature. 43 This peak position is likely caused by the asymmetric stretching mode of planar skeletal Si<sub>3</sub>N bonds, which is found in the frequency range 800-950 cm<sup>-1</sup>. This observation of Si-rich SiN<sub>x</sub> can be explained by the low nitrogen reactivity in the plasma at low plasma powers, leading to an insufficient number of N atoms to form Si-N bonds. The observation of Si-rich  $SiN_x$  at low power is also consistent with the low transparency of these films, as observed in Figures 2 and 3.

As Figure 4b shows, for plasma powers between 10 and 60 W, the absorption peak inside the atmospheric transmission window gradually shifts toward higher wavenumbers, which is indicative of increasing N content in the particle film. This can easily be explained by an increase in atomic nitrogen production inside the plasma due to high input plasma power. However, for plasma powers of 70 to 90 W, we see a sudden emergence of a shoulder between 1000 and 1100 cm<sup>-1</sup>, which is associated with  $N_3-(Si-N)-Si_2$  or  $SiN_4$  bonding. The emergence of this shoulder is unexpected, since it does not correlate to changes in plasma chemistry between 50 and 90 W, as will be described in section 3.3. However, the

**ACS Applied Optical Materials** 

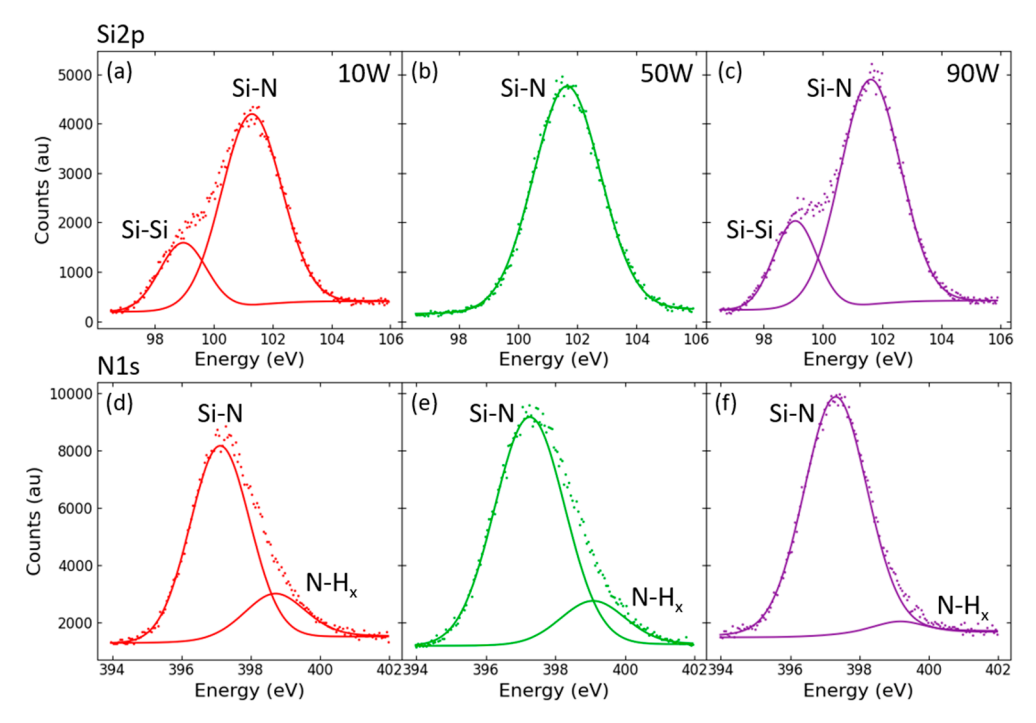


Figure 5. High resolution XPS spectra of the silicon 2p and nitrogen 1s orbitals of samples deposited at (a, d) 10, (b, e) 50, and (c, f) 90 W.

 ${
m SiN_x}$  matrix deformation associated with this absorption feature is well documented to occur as a result of Si nanocrystal precipitation from the amorphous  ${
m SiN_x}$  matrix at higher annealing temperatures around  $1000~{
m C.}^{44-46}$  While the gas temperature in our experiment likely remains close to room temperature, the temperature of NPs inside a plasma is known to be able to exceed the gas temperature by many hundreds of Kelvins, mostly due to electron—ion recombination on the particle surface. The flux of charged particles colliding with the NPs naturally increases with plasma power, and thus so does the NP temperature. Apparently, for plasma powers above 70 W, the NP temperature reaches a value where Si nanocrystal precipitation becomes possible. This also explains the increased absorption of visible light for the films deposited at higher power, as seen in Figure 2.

#### 3.2. Material Characterization

For further examination of the chemical composition of the deposited NP films, XPS was performed on the samples deposited at 10, 50, and 90 W of plasma power. Figure 5 shows high resolution XPS spectra of silicon 2p and nitrogen 1s bonds within the samples. The top three panels show the Si 2p peaks, and the bottom three panels show the N 1s peaks at 10, 50, and 90 W of plasma power, respectively.

Figure 5a, corresponding to the 10 W sample, shows two peaks: a Si–N peak at 101.3 eV and a metallic Si(0) peak at 99 eV. The metallic peak is likely caused by amorphous grouping of elemental silicon within the silicon-nitride matrix confirming the 10 W sample to be a Si-rich SiN<sub>x</sub>. <sup>48</sup> The formation of Sirich SiN<sub>x</sub> at 10 W suggests that there is insufficient atomic nitrogen, or high-vibrational temperature N<sub>2</sub>, at low powers to bond with Si radicals within the plasma. Figure 5d shows the nitrogen 1s orbital for the 10 W sample, wherein we observe a strong peak at 397 eV, which corresponds to Si–N bonding, and a less pronounced feature at 399 eV, corresponding to N–H bonding. Thus, the XPS results for the 10 W sample are in good agreement with our previous hypothesis of insufficient

nitrogen being incorporated into the sample at low powers, thus yielding silicon-rich SiN<sub>v</sub>.

Figure 5b shows the silicon 2p orbital for the 50 W sample. In contrast to the film deposited at 10 W, it shows only a single peak at 101 eV that corresponds to Si-N species in the SiN<sub>x</sub> film. The disappearance of the metallic Si peak, that was observed at 10 W, is likely caused by the increased nitrogen concentration in the particle film, favoring Si-N bond formation over Si-Si bonds. Furthermore, the N 1s peak shown in Figure 5e shows a slightly stronger Si-N peak at 397 eV and a slightly weaker N-H peak at 399 eV. It is vital to note that an increase in N-H bonding is not seen at higher powers. This contrasts with other gas-phase SiN<sub>x</sub> synthesis techniques which mostly use NH3 concentration as the nitrogen content tuning parameter. 23 In these studies, an increase in NH3 will inherently allow for an increase in hydrogen content, which is known to degrade many material properties including IR transparency.

At 90 W, Figure 5c shows the re-emergence of the metallic Si–Si peak observed at 10 W but missing at 50 W. As XPS will not distinguish between amorphous and crystalline structures, it is expected that amorphous and crystalline Si–Si bonding will appear identical. Thus, this peak agrees with the hypothesis of silicon nanocrystal precipitation at higher powers, as previously discussed. Figure 5f shows a similar pattern seen in the N 1s bonding from 10 to 50 W of plasma power. A slight increase in Si–N bonding peak height is seen along with a slight decrease in N–H bonding peak. This pattern further supports the correlation between the nitrogen content within the material and plasma power, which will be explored in section 3.3.

Compositional percentages were calculated yielding Si/N ratios of 86.6%, 75.8%, and 86.4% for the 10, 50, and 90 W samples, respectively. The 10 and 50 W samples have Si/N ratios that agree with previous characterization indicating silicon rich and stoichiometric compositions (Si/N = 75% for  $Si_3N_4$ ). The Si/N ratio at 90 W, at face value, indicates a return

to Si-rich silicon nitride due to the re-emergence of metallic silicon bonding. However, under the hypothesized precipitation of SI nanocrystals, a two-phase material (Si nanocrystals and N-rich  $\mathrm{SiN}_x$ ) would be formed, with XPS being unable to distinguish between these two phases. Furthermore, we hypothesize that as the Si–N bonds are separated within the nitrogen-rich  $\mathrm{SiN}_x$ ,  $\mathrm{N}_2$  can form and thus no longer is part of the material. This hypothesis suggests that  $\mathrm{N}_2$  outgassing is possible and therefore could explain the higher-than-expected  $\mathrm{Si/N}$  ratio seen in the sample deposited at 90 W of plasma power.

It should be noted that FTIR and XPS measurements were performed without the samples being exposed to the atmosphere to prevent oxidation. SiN, thin films are known to begin to oxidize immediately when exposed to the atmosphere. However, certainly as PRC films, these  $SiN_x$ NPs will oxidize and to become silicon oxynitride  $(SiN_xO_y)$ NP films, but this oxidation does not inhibit the potential use as a PRC device as SiN<sub>x</sub>O<sub>y</sub> is known to be an amorphous material with optical properties between SiO<sub>2</sub> and SiN<sub>3</sub>. To ensure that IR emission in the atmospheric transmission window and minimized visible absorption are stable in atmosphere, we set the 50 W sample out in ambient conditions for 30 days to allow for atmospheric oxidation to occur. After 30 days we measured IR and visible absorption with FTIR and UV-vis again (see Supporting Information Figure S2). We observed a strong Si-O absorption feature in the atmospheric transmission window and minor absorption features growing outside of the atmospheric transmission window. We also saw a minor absorption increase of <5% from 350 to 500 nm. These minor optical absorption onsets from oxidation would indeed degrade the overall cooling potential of a PRC device. This is likely due to particle decomposition from atmosphere exposure. However, more importantly, the strong emission features in the atmospheric transmission window remained while also maintaining high visible transparency.

To confirm the hypothesis of Si nanocrystal precipitation at higher powers, we performed TEM imaging of the 90 W SiN $_x$  NP sample. Figure 6 shows a bright field TEM image of a sparsely deposited sample at 90 W, obtained at a deposition time of 0.5 s. Careful examination of the lattice fringes seen within the nanoparticles reveals the formation of crystalline Si with a lattice spacing of 0.31 nm. This value is consistent with the (111) peak of crystalline Si, confirming our hypothesis of Si nanocrystal precipitation at high plasma powers. However, it should be noted that only parts of the nanoparticles show clear signs of crystallization, while the rest of the particle remains amorphous, nitrogen-rich SiN $_x$ . The inset of the figure shows the corresponding SAED pattern, revealing Si (111), (220), and (311) diffraction rings (PDF number: 027–1402).

## 3.3. Process Characterization

Optical emission spectroscopy (OES) was performed to characterize the synthesis process and explain the trends observed in the material properties of the deposited NP films with varying plasma power.

To extract useful information about the plasma from the observed emission line and band intensities, it is helpful to discuss the measurements in the context of the corona model, even if this is a strong simplification in the case of our plasma. In the corona model, the intensity of an optical emission line  $I_m$  is proportional to the electron density  $n_e$ , the density of the emitting atom, ion, or molecule  $n_m$  and the excitation rate

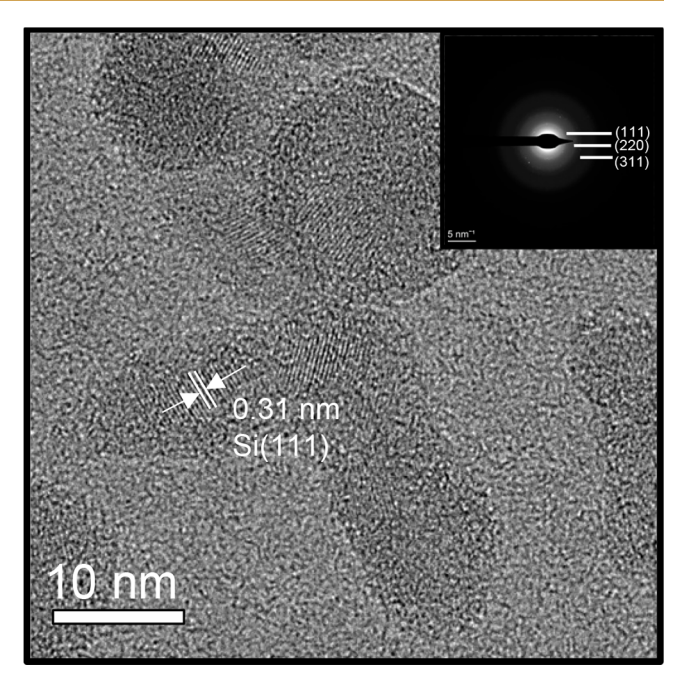


**Figure 6.** TEM image showing nanocrystal formation within the sample deposited at 90 W of power. Lattice spacing was observed to match with the silicon (111) plane.

from the ground state  $X_m$ , which in turn is a function of the electron energy distribution function  $f_e$  (EEDF).<sup>51</sup>

$$I_m \propto n_e n_m X_m (f_e) \tag{1}$$

Here,  $X_m$  usually increases strongly with the mean electron energy so that the brightness of optical emission lines mostly follows trends in electron energy.

As shown in Figure 7a, the intensity of Si I quickly drops between 10 and 30 W while staying approximately constant for higher plasma powers. This indicates a reduction of silane density between at least 10 and 30 W, caused by particle formation, which naturally uses up the available Si precursor. This trend is reflected in the Ar I emission, which initially decreases between 10 and 30 W and then increases again for higher powers. This intensity minimum around 30 W cannot be caused by changes in emitter density since we supply the reactor with a constant stream of argon and the noble gas will barely react with other species. The excitation rate can also be excluded as the cause for the minimum since any increase in power is expected to only increase the mean electron density. Consulting eq 1, the Ar I intensity minimum must therefore be caused by a reduction in electron density.

Such an electron density reduction again points to increased NP formation with power between 10 and 30 W: as the particle density increases, the plasma becomes increasingly electronegative, leading to a reduction in electron density. Additionally, the plasma will adjust to the increased losses of charged species to the NPs by an increase in the average electron energy, thus also increasing the excitation rate. That we still observe a minimum in Ar I emission hints at the electron density depletion being quite severe under these conditions.

For plasma powers above 40 W, the Ar I emission intensity increases almost linearly with power. This fits our assumption that the precursor has been used up for particle formation at these powers, leading to an about constant particle density

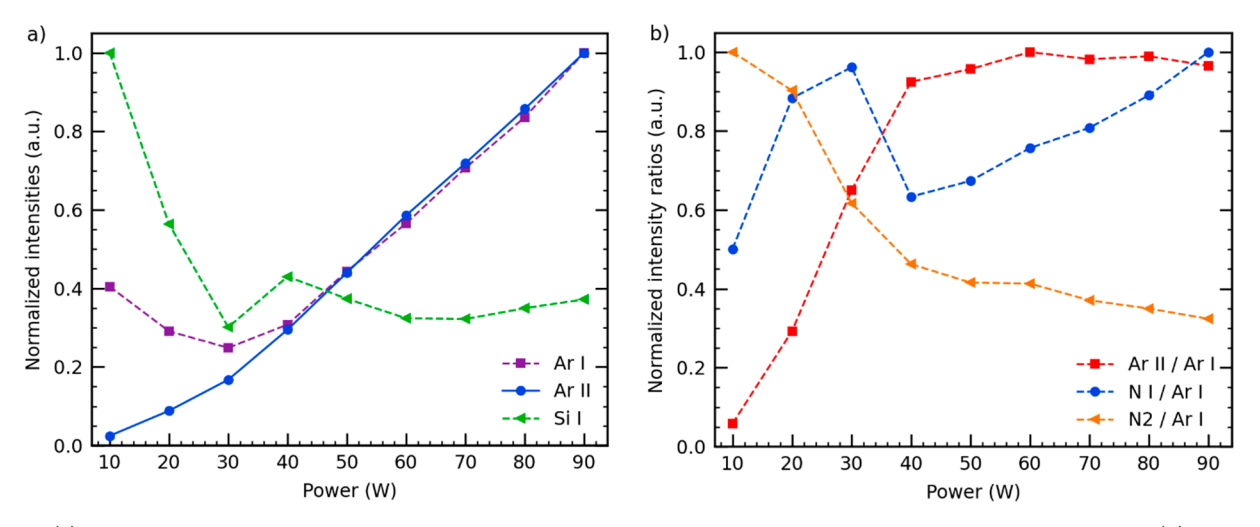


Figure 7. (a) Normalized line intensities of emission from argon neutrals, argon ions, and silicon neutrals as a function of power. (b) Normalized line intensity ratios of emission from diatomic nitrogen, atomic nitrogen, and argon ions as compared to argon neutrals emission.

inside the plasma for powers above 40 W. Thus, the increase in power now simply yields increased electron densities and temperatures, causing increased emission.

In contrast to the Si I and Ar I trends, Ar II emission steadily increases with power. This is because the density of argon ions is increasing as a function of power, even as the electron density seems to decrease between 10 and 30 W. This increase in emitter density overcompensates the electron density minimum around 30 W, even if we do see a slightly slower Ar II increase between 10 and 30 W.

Summarizing our discussion of Figure 7a, we find that between 10 and maybe 40 W, an increase in plasma power leads to an increase in nanoparticle production and density, causing a reduction in silane density. Between 10 W and at least 30 W, the electron density decreases as a function of power. For higher powers, the Si precursor is all used up leading to a constant particle mass density.

We will now consider line ratios of different species normalized to the emission of Ar I, as shown in Figure 7b. As demonstrated by eq 1, these line ratios should be independent of electron density, and the dependence on electron energies should be much reduced. As such, we will assume the line ratios to roughly represent emitter density ratios. Since the density of argon neutrals is approximately constant, density changes for argon ions, nitrogen atoms (N I) and molecules  $(N_2)$  can be observed.

We will first regard the trend in the Ar II intensity ratio which shows a strong increase between 10 and 40 W and is then approximately constant for higher powers. This constant Ar II intensity ratio for higher plasma power can be explained by an expansion of the plasma volume, as was observed for powers above 40 W. Part of the increased power will be used up in expanding the plasma volume instead of increasing the ion density, leading to an approximately constant Ar II intensity ratio for higher plasma powers.

For molecular nitrogen, we find a steady decrease with power. This decrease might be caused by an increase in the dissociation rate, reducing the density of molecular nitrogen. However, molecular nitrogen can also be efficiently excited by collisions with argon metastable, so that the observed trends will also be affected by changes in argon metastable densities. <sup>52</sup> Initially, the decrease in molecular nitrogen signal is quick, as the plasma turns more electronegative, the average electron

energy strongly increases. For higher powers, the increase in electron energy is slower, leading to a slower reduction in  $N_2$  signal with power.

For atomic nitrogen, the situation is more complicated since we need to consider not only the production from molecular nitrogen but also the different reaction pathways decreasing the atomic nitrogen density. Notable loss mechanisms are volume reactions with hydrogen species, forming  $\mathrm{NH}_{xv}$ , recombination to  $\mathrm{N}_2$ , as well as the desired surface reactions on the particles, forming silicon nitride. As such, the increase in atomic nitrogen signal between 10 and 30 W, as well as 40 and 90 W might simply be understood as the result of an increase in molecular nitrogen dissociation rate. However, the strong reduction between 30 and 40 W is more challenging to explain. It should be noted that a sizable part of the emission line intensity of N I might be caused by dissociative excitation, in which case the relationship between the emission line intensity and emitter density becomes much more complicated.

Based on these observations about the emission intensity of molecular and atomic nitrogen, a monotonous increase of atomic nitrogen production with power seems likely. For the reactivity of molecular nitrogen, the trend is unclear since the vibrational temperature (not shown) of  $N_2$  peaks at 30 W at 5800 K and then decreases with power to 4800 K at 90 W. However, NP temperatures should be increasing with power above 30 W, as a larger flux of charged species reaches the particles. It is unknown whether the surface temperature of the particles or the vibrational temperature of the molecules is more important for the formation of Si–N bonds from diatomic nitrogen under these conditions.

For low power, the Si precursor is not completely transformed into particles in the observed volume. Particle production may continue downstream closer to the extraction nozzle. There, however, we expect a low atomic nitrogen concentration and vibrational and surface temperature, so that the resulting particles end up with under-stoichiometric nitrogen concentrations, as our XPS results confirm. Consequently, the NP films are not transparent at these powers, as Figures 2 and 3 demonstrate. For powers between 40 and 90 W, particles are formed in the observed region or above so that the overall nitrogen reactivity for particle formation can be tuned using the plasma power.

#### 4. CONCLUSIONS

 ${\rm SiN_x}$  nanoparticle films were deposited from a nonthermal plasma reactor using a fixed gas mixture of  ${\rm SiH_4}$ ,  ${\rm N_2}$ , and Ar, at powers ranging from 10 to 90 W. The nitrogen content inside the nanoparticles could be tuned with increasing plasma power forming composition tunable  ${\rm SiN_x}$  NP films. The film deposited at low powers featured an under-stoichiometric concentration of nitrogen, while at high powers, nanoparticle heating led to Si nanocrystal precipitation. However, at 50 W, films of stoichiometric  ${\rm Si_3N_4}$  nanoparticles were achieved. These films were shown to be highly transparent in the visible range while at the same time showing strong emissivity in the atmospheric transmission window. These features make the films ideal passive radiative cooling devices. Measurements of the experimental cooling power of the deposited films will be performed in the future.

## ASSOCIATED CONTENT

## Supporting Information

The Supporting Information is available free of charge at https://pubs.acs.org/doi/10.1021/acsaom.3c00257.

SEM figures of  $SiN_x$  samples and FTIR and absorption spectra of oxidized  $SiN_x$  samples (PDF)

## AUTHOR INFORMATION

#### **Corresponding Author**

Uwe Kortshagen — Department of Mechanical Engineering, University of Minnesota, Minneapolis, Minnesota 55455, United States of America; ⊚ orcid.org/0000-0001-5944-3656; Email: kortshagen@umn.edu

## **Authors**

- Gunnar Nelson Department of Mechanical Engineering, University of Minnesota, Minneapolis, Minnesota 55455, United States of America
- Himashi P. Andaraarachchi Department of Mechanical Engineering, University of Minnesota, Minneapolis, Minnesota 55455, United States of America; orcid.org/0000-0001-9736-1088
- Mohammad Ali Eslamisaray Department of Mechanical Engineering, University of Minnesota, Minneapolis, Minnesota 55455, United States of America; ⊚ orcid.org/0000-0001-8704-592X
- Ognjen Ilic Department of Mechanical Engineering, University of Minnesota, Minneapolis, Minnesota 55455, United States of America; orcid.org/0000-0001-8651-7438

Complete contact information is available at: https://pubs.acs.org/10.1021/acsaom.3c00257

## **Funding**

G. Nelson acknowledges support by the National Science Foundation Graduate Research Fellowship Program under Grant No. 1839286. G. Nelson, H. Andaraarachchi, and U. Kortshagen acknowledge support by the U.S. Army Research Office under MURI Grant W911NF-18-1-0240. This work was supported by the U.S. National Science Foundation through

the University of Minnesota MRSEC under Award Number DMR-2011401. Parts of this work were carried out in the Characterization Facility, University of Minnesota, which receives partial support from NSF through the MRSEC program.

#### **Notes**

The authors declare no competing financial interest.

## REFERENCES

- (1) IEA. The Future of Cooling; IEA: Paris, 2018.
- (2) Zhao, B.; Hu, M.; Ao, X.; Chen, N.; Pei, G. Radiative cooling: A review of fundamentals, materials, applications, and prospects. *Applied Energy* **2019**, 236, 489–513.
- (3) Hossain, Md. M.; Gu, M. Radiative Cooling: Principles, Progress, and Potentials. *Adv. Sci.* **2016**, *3*, 1500360.
- (4) Li, Z.; Chen, Q.; Song, Y.; Zhu, B.; Zhu, J. Fundamentals, Materials, and Applications for Daytime Radiative Cooling. *Adv. Mater. Technol.* **2020**, *5*, 1901007.
- (5) Lu, X.; Xu, P.; Wang, H.; Yang, T.; Hou, J. Cooling potential and applications prospects of passive radiative cooling in buildings: The current state-of-the-art. *Renewable and Sustainable Energy Reviews* **2016**, *65*, 1079–97.
- (6) Raman, A. P.; Anoma, M. A.; Zhu, L.; Rephaeli, E.; Fan, S. Passive radiative cooling below ambient air temperature under direct sunlight. *Nature* **2014**, *S15*, 540–4.
- (7) Yin, X.; Yang, R.; Tan, G.; Fan, S. Terrestrial radiative cooling: Using the cold universe as a renewable and sustainable energy source. *Science* **2020**, *370*, 786–91.
- (8) Zeyghami, M.; Goswami, D. Y.; Stefanakos, E. A review of clear sky radiative cooling developments and applications in renewable power systems and passive building cooling. *Sol. Energy Mater. Sol. Cells* **2018**, *178*, 115–28.
- (9) Granqvist, C. G.; Hjortsberg, A.; Eriksson, T. S. Radiative cooling to low temperatures with selectivity IR-emitting surfaces. *Thin Solid Films* **1982**, *90*, 187–90.
- (10) Rephaeli, E.; Raman, A.; Fan, S. Ultrabroadband Photonic Structures To Achieve High-Performance Daytime Radiative Cooling. *Nano Lett.* **2013**, *13*, 1457–61.
- (11) Hossain, M. M.; Jia, B.; Gu, M. A Metamaterial Emitter for Highly Efficient Radiative Cooling. *Advanced Optical Materials* **2015**, 3, 1047–51.
- (12) Wray, P. R.; Su, M. P.; Atwater, H. A. Design of efficient radiative emission and daytime cooling structures with Si  $_3$  N  $_4$  and SiO  $_2$  nanoparticle laminate films. *Opt. Express* **2020**, *28*, 35784.
- (13) Krogman, K. C.; Druffel, T.; Sunkara, M. K. Anti-reflective optical coatings incorporating nanoparticles. *Nanotechnology* **2005**, *16*, \$338–43.
- (14) Moghal, J.; Kobler, J.; Sauer, J.; Best, J.; Gardener, M.; Watt, A. A. R.; Wakefield, G. High-performance, single-layer antireflective optical coatings comprising mesoporous silica nanoparticles. *ACS Appl. Mater. Interfaces* **2012**, *4*, 854–9.
- (15) Evlyukhin, A. B.; Reinhardt, C.; Seidel, A.; Luk'yanchuk, B. S.; Chichkov, B. N. Optical response features of Si-nanoparticle arrays. *Phys. Rev. B* **2010**, *82*, 045404.
- (16) Choy, T C Effective Medium Theory: Principles and Applications; Clarendon Press: Oxford, 2007.
- (17) Markel, V. A. Introduction to the Maxwell Garnett approximation: tutorial. *J. Opt. Soc. Am. A* **2016**, 33, 1244.
- (18) Trewyn, B. G.; Slowing, I. I.; Giri, S.; Chen, H.-T.; Lin, V S-Y Synthesis and Functionalization of a Mesoporous Silica Nanoparticle Based on the Sol-Gel Process and Applications in Controlled Release. *Acc. Chem. Res.* **2007**, *40*, 846–53.
- (19) Tang, F.; Li, L.; Chen, D. Mesoporous Silica Nanoparticles: Synthesis, Biocompatibility and Drug Delivery. *Adv. Mater.* **2012**, *24*, 1504–34.
- (20) Wu, S.-H.; Mou, C.-Y.; Lin, H.-P. Synthesis of mesoporous silica nanoparticles. *Chem. Soc. Rev.* **2013**, 42, 3862.

- (21) Hegedüs, N.; Balázsi, K.; Balázsi, C. Silicon Nitride and Hydrogenated Silicon Nitride Thin Films: A Review of Fabrication Methods and Applications. *Materials* **2021**, *14*, 5658.
- (22) Kaloyeros, A. E.; Pan, Y.; Goff, J.; Arkles, B. Review—Silicon Nitride and Silicon Nitride-Rich Thin Film Technologies: State-of-the-Art Processing Technologies, Properties, and Applications. ECS J. Solid State Sci. Technol. 2020, 9, 063006.
- (23) Riley, F. L. Silicon Nitride and Related Materials. J. Am. Ceram. Soc. 2000, 83, 245–65.
- (24) Chae, S.; Park, S.; Ahn, K.; Nam, G.; Lee, T.; Sung, J.; Kim, N.; Cho, J. Gas phase synthesis of amorphous silicon nitride nanoparticles for high-energy LIBs. *Energy Environ. Sci.* **2020**, *13*, 1212–21.
- (25) Kilian, S. O.; Wiggers, H. Gas-Phase Synthesis of Silicon-Rich Silicon Nitride Nanoparticles for High Performance Lithium-Ion Batteries. *Part. Part. Syst. Charact.* **2021**, *38*, 2100007.
- (26) Kortshagen, U. R.; Sankaran, R. M.; Pereira, R. N.; Girshick, S. L.; Wu, J. J.; Aydil, E. S. Nonthermal plasma synthesis of nanocrystals: Fundamental principles, materials, and applications. *Chem. Rev.* **2016**, *116*, 11061–127.
- (27) Bapat, A.; Anderson, C.; Perrey, C. R.; Carter, C. B.; Campbell, S. A.; Kortshagen, U. Plasma synthesis of single-crystal silicon nanoparticles for novel electronic device applications. *Plasma Phys. Control. Fusion* **2004**, *46*, B97–109.
- (28) Holman, Z. C.; Kortshagen, U. R. A flexible method for depositing dense nanocrystal thin films: impaction of germanium nanocrystals. *Nanotechnology* **2010**, *21*, 335302.
- (29) Hunter, K. I.; Andaraarachchi, H. P.; Kortshagen, U. R. Nonthermal plasma synthesized silicon-silicon nitride core-shell nanocrystals with enhanced photoluminescence. *J. Phys. D: Appl. Phys.* **2021**, *54*, 504005.
- (30) Mandal, R.; O'Shea, K.; Anthony, R. Silicon nitride-capped silicon nanocrystals via a nonthermal dual-plasma synthesis approach. *Journal of Vacuum Science & Technology A* **2018**, *36*, 051303.
- (31) Zhou, H.; Elgaid, K.; Wilkinson, C.; Thayne, I. Low-Hydrogen-Content Silicon Nitride Deposited at Room Temperature by Inductively Coupled Plasma Deposition. *Jpn. J. Appl. Phys.* **2006**, 45, 8388–92.
- (32) Luongo, J. P. IR Study of Amorphous Silicon Nitride Films. Appl. Spectrosc. 1984, 38, 195–9.
- (33) Mangolini, L.; Thimsen, E.; Kortshagen, U. High-Yield Plasma Synthesis of Luminescent Silicon Nanocrystals. *Nano Lett.* **2005**, *5*, 655–9.
- (34) Xiong, Z.; Lanham, S.; Husmann, E.; Nelson, G.; Eslamisaray, M. A.; Polito, J.; Liu, Y.; Goree, J.; Thimsen, E.; Kushner, M. J.; Kortshagen, U. R. Particle trapping, size-filtering, and focusing in the nonthermal plasma synthesis of sub-10 nm particles. *J. Phys. D: Appl. Phys.* **2022**, 55, 235202.
- (35) Rueden, C. T.; Schindelin, J.; Hiner, M. C.; DeZonia, B. E.; Walter, A. E.; Arena, E. T.; Eliceiri, K. W. ImageJ2: ImageJ for the next generation of scientific image data. *BMC Bioinformatics* **2017**, *18*, 529
- (36) Voráč, J.; Kusýn, L.; Synek, P. Deducing rotational quantumstate distributions from overlapping molecular spectra. *Rev. Sci. Instrum.* **2019**, *90*, 123102.
- (37) Voráč, J.; Synek, P.; Potočňáková, L.; Hnilica, J.; Kudrle, V. Batch processing of overlapping molecular spectra as a tool for spatio-temporal diagnostics of power modulated microwave plasma jet. *Plasma Sources Sci. Technol.* **2017**, *26*, 025010.
- (38) Voráč, J.; Synek, P.; Procházka, V.; Hoder, T. State-by-state emission spectra fitting for non-equilibrium plasmas: OH spectra of surface barrier discharge at argon/water interface. *J. Phys. D: Appl. Phys.* **2017**, *50*, 294002.
- (39) Mohamed Okasha Mohamed Okasha, A.; Kafle, B.; Torda, B.; Teßmann, C.; Hofmann, M. Optimized amorphous silicon nitride layers for the front side passivation of c-Si PERC solar cells. *EPJ. Photovolt.* **2020**, *11*, 6.
- (40) DiGregorio, S. N.; Habermehl, S. D. Infrared absorption cross section of SiNx thin films. *Journal of Vacuum Science & Technology A* **2020**, 38, 013404.

- (41) Liu, F.; Ward, S.; Gedvilas, L.; Keyes, B.; To, B.; Wang, Q.; Sanchez, E.; Wang, S. Amorphous silicon nitride deposited by hotwire chemical vapor deposition. *J. Appl. Phys.* **2004**, *96*, 2973–9.
- (42) Liu, C.-Y.; Kortshagen, U. R. A Silicon Nanocrystal Schottky Junction Solar Cell produced from Colloidal Silicon Nanocrystals. *Nanoscale Res. Lett.* **2010**, *5*, 1253–6.
- (43) Kato, I.; Numada, K.; Kiyota, Y. Oxidation Properties of Silicon Nitride Thin Films Fabricated by Double Tubed Coaxial Line Type Microwave Plasma Chemical Vapor Deposition. *Jpn. J. Appl. Phys.* **1988**, *27*, 1401–5.
- (44) Scardera, G.; Puzzer, T.; Conibeer, G.; Green, M. A. Fourier transform infrared spectroscopy of annealed silicon-rich silicon nitride thin films. *J. Appl. Phys.* **2008**, *104*, 104310.
- (45) Debieu, O.; Nalini, R. P.; Cardin, J.; Portier, X.; Perrière, J.; Gourbilleau, F. Structural and optical characterization of pure Si-rich nitride thin films. *Nanoscale Res. Lett.* **2013**, *8*, 31.
- (46) Bustarret, E.; Bensouda, M.; Habrard, M. C.; Bruyère, J. C.; Poulin, S.; Gujrathi, S. C. Configurational statistics in *a* Si x N y H z alloys: A quantitative bonding analysis. *Phys. Rev. B* **1988**, 38, 8171–84
- (47) Mangolini, L.; Kortshagen, U. Selective nanoparticle heating: Another form of nonequilibrium in dusty plasmas. *Phys. Rev. E* **2009**, 79, 026405.
- (48) Nguyen, S. V.; Fridmann, S. Plasma Deposition and Characterization of Thin Silicon-Rich Silicon Nitride Films. *J. Electrochem. Soc.* **1987**, *134*, 2324–9.
- (49) Liao, W.; Lin, C.; Lee, S. Oxidation of silicon nitride prepared by plasma-enhanced chemical vapor deposition at low temperature. *Appl. Phys. Lett.* **1994**, *65*, 2229–31.
- (50) Viard, J.; Beche, E.; Perarnau, D.; Berjoan, R.; Durand, J. XPS and FTIR study of silicon oxynitride thin films. *J. Eur. Ceram. Soc.* 1997, 17, 2025–8.
- (51) Kunze, H.-J. Introduction to Plasma Spectroscopy; Springer: Berlin, 2009.
- (52) Hattangady, S. V.; Fountain, G. G.; Rudder, R. A.; Markunas, R. J. Low hydrogen content silicon nitride deposited at low temperature by novel remote plasma technique. *Journal of Vacuum Science & Technology A: Vacuum, Surfaces, and Films* **1989**, 7, 570–5.